Optical calculation of potential fields for robotic path planning

Max B. Reid

Optical calculation of potential fields for robotic path planning

Max B. Reid

Experimental results of the optical calculation of potential-field maps suitable for mobile robot navigation are presented and described. The optical computation employs two write modes of a microchannel spatial light modulator. In one mode, written patterns expand spatially, and this characteristic is used to create an extended two-dimensional function representing the influence of the goal in a robot's workspace. Distinct obstacle patterns are written in a second, nonexpanding, mode. A model of the mechanisms determining microchannel spatial light modulator write-mode characteristics is developed and used to derive the optical calculation time for full potential-field maps. Field calculations at a few hertz are possible with current technology, and calculation time versus map size scales favorably in comparison with digital electronic computation.

1. Introduction

The microchannel spatial light modulator (MSLM) is a versatile device capable of a number of different operating modes. Originally developed to implement continuous-phase modulation,[1,2] its operation was later extended to include gray-scale amplitude modulation, image addition and subtraction, intensity-level thresholding, and binary logic operations.[2-4] Commercial versions of the MSLM[5-7] have been utilized in a variety of optical processing applications.[8-11]

A diagram of the MSLM is shown in Fig. 1. The device consists essentially of a photocathode, a microchannel plate (MCP), a mesh electrode, and an electro-optic crystal. An input light intensity distribution is converted by the photocathode to a spatial electronic current distribution, which is then amplified of the order of 1000 times by the MCP and deposited on the crystal, typically $LiNbO_3$. The electro-optic crystal is coated with a thin dielectric mirror, typically of either SiO_2 or SiO_2/ZrO_2 multilayer.[7] A charge from the MCP accumulates on the surface of the mirror, with the charge density increasing in proportion to the spatial intensity distribution of the input write light incident upon the photocathode. The deposited surface charge density, σ_s, creates an electric field across the electro-optic crystal. The polarization of a coherent readout light beam that passes twice through the electro-optic crystal is rotated by this electric field by means of the Pockels effect,[12] and the spatial distribution in σ_s is converted to an intensity distribution in the readout beam through the use of an analyzer.

There are two basic methods that can be used to write spatial patterns onto the MSLM. The first is through electron deposition onto the dielectric mirror, as described above. The second method involves first depositing a uniform charge distribution on the surface of the mirror and then removing, or depleting, charge from areas to be written. Figures 2(a) and 2(b) show the results of writing a simple square pattern in the two modes. In both cases the pattern was written up to a point of ~90% modulation, requiring writing times of t_1 and t_2 for the deposition and the depletion modes, respectively. At this level of modulation the two written patterns are very nearly reverse contrast images of each other. However, if the electron deposition and depletion process is continued beyond ~90% modulation, the two patterns begin to differ considerably, as shown in Figs. 2(c) and 2(d), in which the deposited pattern is written for $3t_1$ and the depleted pattern for a time $3t_2$. If writing is continued, the deposited pattern grows to fill the entire active area of the electro-optic crystal, while the depleted pattern remains relatively confined.

The spread of spatial patterns written in deposition mode has not been discussed at any length in the MSLM literature. It has been considered an artifact to be avoided either by discontinuation of deposition writing before full modulation is reached[2-4] or by
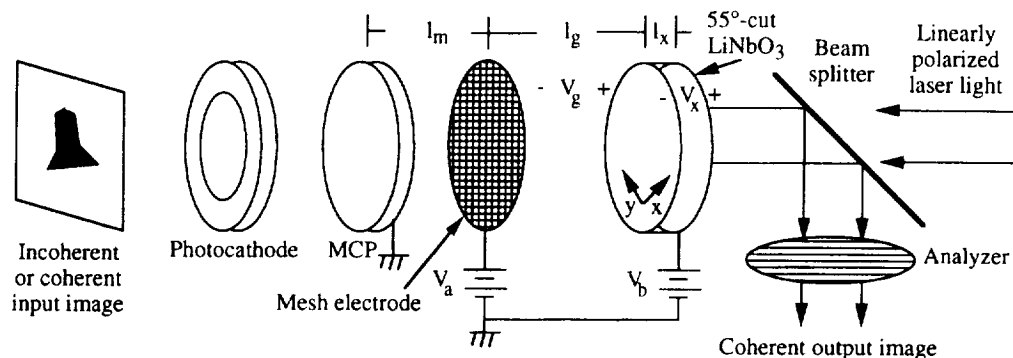
Fig. 1. Basic operation of the microchannel spatial light modulator: V_a, voltage applied to the mesh electrode; V_b, voltage applied to the crystal; V_g, gap voltage; V_x, voltage drop across the crystal.

restriction of the MSLM use to the electron-depletion write mode. In this paper I wish to demonstrate that the spatial spread of charge across the surface of the electro-optic crystal may have practical application, permitting analog calculation of complicated two-dimensional spatial functions that are **very** time consuming to compute with standard digital techniques. The particular application considered here is the calculation of two-dimensional potential-field maps suitable for use in autonomous robotic path planning.

The remainder of this paper is divided into six sections. Section 2 reviews the basic operation of the MSLM and shows how the inclusion of transverse effects can explain the spatial spread of patterns written with electron deposition. Section 3 describes the use of potential-field maps for robotic path planning. Algorithms are described that involve a potential well centered at the location of a robot's goal state, high-potential obstacles that a robot must avoid, and techniques for calculating potentials for all

other locations such that the robot is attracted from any initial position to the goal.

Optical techniques for representing goals and obstacles and for calculating intervening potential-field values are presented in Section 4. The time required for performance of optical calculation of a full-potential field map is derived in Section 5 and is compared with current digital techniques. Examples of experimentally calculated potential fields and the paths that simulated robots follow through the obstacles are presented in Section 6, and conclusions are given in Section 7.

2. Microchannel Spatial Light Modulator Operation

The principles of MSLM operation are well described in the literature[1] [7] and are only summarized here. A diagram of the key components and dimensions is shown in Fig. 3.[4] Electrons leaving the MCP output electrode are accelerated by the grid electrode to potential V_a, which is of the order of 2 kV. The initial energies of the electrons as they leave the MCP are only a few electron volts or a few tens of electron volts,[13] so the energy of primary electrons striking the dielectric mirror is well approximated by

$$E_p = e(V_a + V_g), \qquad (1)$$

where e is the electron charge and the gap voltage is given by

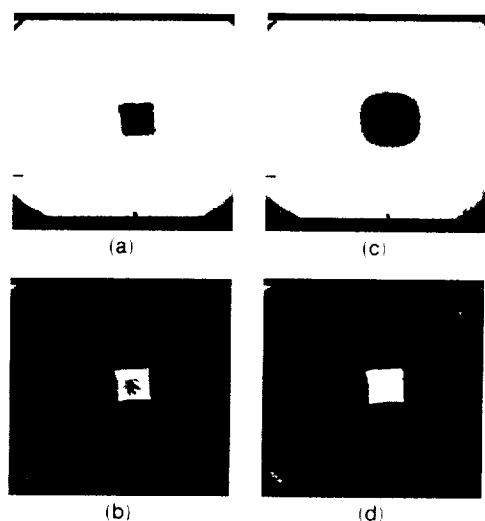$$V_g = V_b - V_a - V_x, \qquad (2)$$

Fig. 2. Behavior of electron-deposition and electron-depletion writing modes: (a) square pattern written for time t_1 to 90% modulation in deposition mode, (b) same pattern written for time t_2 to 90% modulation in depeletion mode, (c) pattern written for $3t_1$ in deposition mode, (d) pattern written for $3t_2$ in depeletion mode.
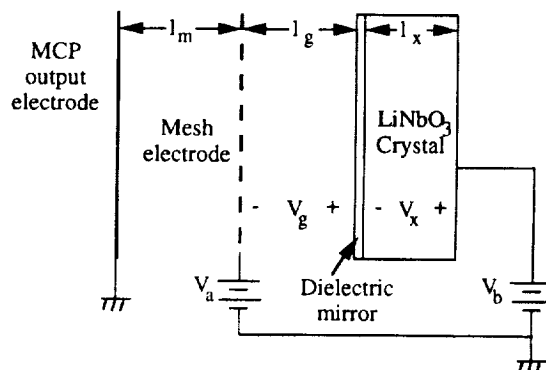

Fig. 3. Key components, dimensions, and voltages of the MSLM.

V_b being the voltage applied to the crystal and V_x being the voltage drop across the crystal caused by accumulated charge on the mirror. In the electron-deposition mode, typical operating values for commercially available Model X1699 MSLM's from Hamamatsu Corporation are $V_a = 1.9$ kV and $V_b = 2.55$ kV, giving $V_g = 650$ V when no charge is deposited on the mirror.

A. Secondary Emission

If only primary electrons emitted from the MCP were involved in the MSLM writing process, charge would accumulate on the mirror until $E_p = 0$ in Eq. (1), requiring $V_x = V_b$. However, on average, each primary electron creates a number, δ_s, of secondary electrons that are emitted from the dielectric-mirror surface. The secondary-emission phenomenon is described in detail in Ref. 14, which is relied on heavily in this section. For primary potentials between the values of V_a and V_b given above, δ_s is always greater than one.

Given $\delta_s > 1$, the net current reaching the mirror would be negative from the relation

$$I_{net} = I_p(1 - \delta_s),\qquad(3)$$

where I_p is the primary-electron current. However, δ_s is reduced to a lower effective value δ_e by the presence of a positive gap voltage, V_g. The energy distribution of secondary electrons is relatively insensitive to E_p for dielectric targets and peaks at fairly low energies of E_s equal to 2 or 3 eV.[14] Therefore the greater majority of secondary electrons are attracted back to the mirror when V_g is of the order of $V_b - V_a$, which is several hundred volts. Only those secondaries with $V_s > V_g$ can cross the gap to be collected on the grid electrode.

This is shown in Fig. 4, which plots both δ_s and δ_e as a function of primary-electron potential, $V_p = V_a + V_g$. When electron deposition begins, $V_g = V_b - V_a$, which is much greater than V_s, so that $\delta_e \approx 0$, $I_{net} \approx I_p$, and charge accumulates on the mirror. A stable equilibrium occurs when $\delta_e = 1$ and $I_{net} = 0$. This

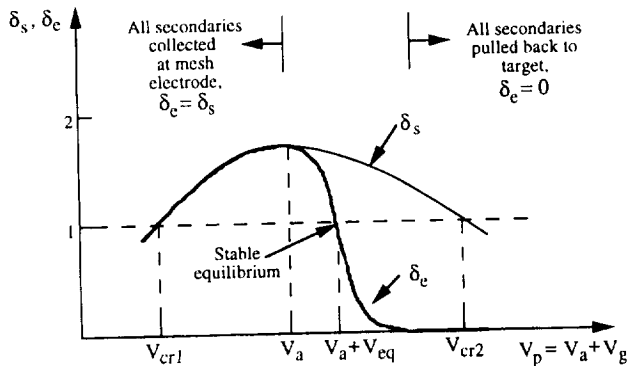equilibrium results when $V_g = V_{eq}$, where V_{eq} is nearly equal to $\langle V_s \rangle$, the mean secondary-electron potential of 2–3 eV.[14] For amplitude modulation, MSLM operating voltages are chosen so that the equilibrium surface charge density is that required to cause a $\pi/2$ phase shift in a readout beam that is reflected off the mirror and passes twice through the crystal, i.e.,

$$\sigma_{s,max} = \sigma_{\pi,2,R}.$$

MSLM operation in electron-depletion mode can also be explained with reference to Fig. 4. With V_a left constant, V_b is dropped so that V_g from Eq. (2) becomes negative. On this part of the curve in Fig. 4, $\delta_e = \delta_s > 1$, and I_{net} from Eq. (3) is negative. Net charge is removed from the mirror until $V_g = V_{eq}$ and $\delta_e = 1$. This writing mode is often referred to as the secondary-emission mode, as it depends on a secondary-electron current that is greater than the primary current leaving the MCP.

The basic MSLM equilibrium model is summarized as follows: for each primary electron striking the dielectric mirror, approximately two secondary electrons are emitted. On average, exactly one of these secondaries has enough energy to reach the grid. Other secondaries have E_s slightly less than $q \cdot V_{eq}$ and are pulled back to the mirror surface. The entire surface is considered to be uniform at the potential $V_a + V_{eq}$, so that no transverse effects are felt.

B. Effect of Transverse Fields

In practice both primary and secondary electrons traversing the gap are affected by the distribution of charge already deposited on the dielectric-mirror surface. At least two mechanisms could lead to the type of pattern expansion seen in Fig. 2: loss of primary focusing and redistribution of secondary electrons.

1. Loss of Primary Focusing

Figure 5 shows the geometry of the situation in which a simple circular pattern of radius ρ is written to the equilibrium potential $V \approx V_a$. The remainder of the

Fig. 4. Secondary-emission coefficient, δ_s, and effective coefficient, δ_e, as a function of primary-electron potential V_p. The two cross-over voltages, V_{cr1} and V_{cr2}, are the primary-electron potentials for which $f_s = 1$.
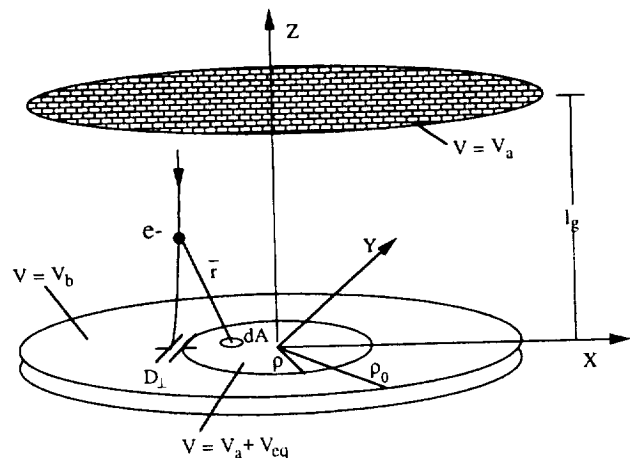

Fig. 5. Geometry for calculation of deflection of primary electrons caused by transverse electric fields on the surface of the dielectric mirror.

MSLM active area, which is a circle with $\rho_0 = 8$ mm, is at V_b. Consider a primary electron leaving the grid with kinetic energy in the direction parallel to the z axis given by $E_{\|0} = q \cdot V_a$, and initial kinetic energy in the transverse plane of $E_{\perp 0} = 0$. The primary that is most deflected from its original trajectory is one aimed at the edge of the pattern, as shown in the figure. We wish to calculate the distance $D_\perp$ by which the primary is displaced from its target. The electric field seen by the electron is given by

$$\overline{E}(z) = \int \frac{\sigma_s \hat{r} \cdot \mathrm{d}\overline{A}}{4\pi\epsilon_0 r^2}, \tag{4}$$

where $\mathrm{d}A$ is an area of deposited charge, r is the distance to the charge, and $\hat{r}$ is the unit vector in the direction from $\mathrm{d}A$ to the primary electron. The surface charge density σ_s is assumed to be the density required to cause a $\pi/2$ phase shift in a readout beam that is reflected off the mirror and that passes twice through the crystal. For a 50-μm-thick 55°-cut LiNbO$_3$ crystal, $\sigma_{\pi\ 2,R} = 4.2 \times 10^{-3}$ C/m^2.[4]

The primary electron's change in velocity after a time t' is given by

$$\overline{v}(t') = \int_0^{t'} \frac{e\overline{E}(t)}{m_e} \, \mathrm{d}t, \tag{5}$$

and the displacement after a time t'' is given by

$$\overline{D}(t'') = \int_0^{t''} \int_0^{t'} \frac{e\overline{E}(t)}{m_e} \, \mathrm{d}t \mathrm{d}t'. \tag{6}$$

Of interest is the transverse component of $\mathbf{D}$ evaluated at time $t'' = t_g$, where t_g is the time required for the electron to traverse the gap. As r is a function of z, which is in turn a function of the electron's velocity, an exact solution to Eq. (6) must be achieved numerically for even very simple geometric patterns of deposited charge. The result for such patterns as the circle in Fig. 5, with ρ equal to a few millimeters and $V_b - V_a = 650$ V, is a transverse displacement $D_\perp$ of 10–100 μm. Such a small displacement results because of the primary's high initial velocity. Indeed, one of the main reasons for including the mesh grid in the construction of the MSLM is to maintain primary focusing.[2-4]

Loss of primary focusing is therefore not the likely cause of the extreme growth in the deposition region shown in Fig. 2, in which the pattern spreads many millimeters beyond the edge of the primary beam. A much more likely cause is the redistribution of secondary electrons.

2. Secondary Redistribution

Secondary electron redistribution results when a secondary emitted from one spot on a target is attracted by transverse fields to another location on the target instead of either being collected on the grid or returned to the location of its emission.[14] Figure 6
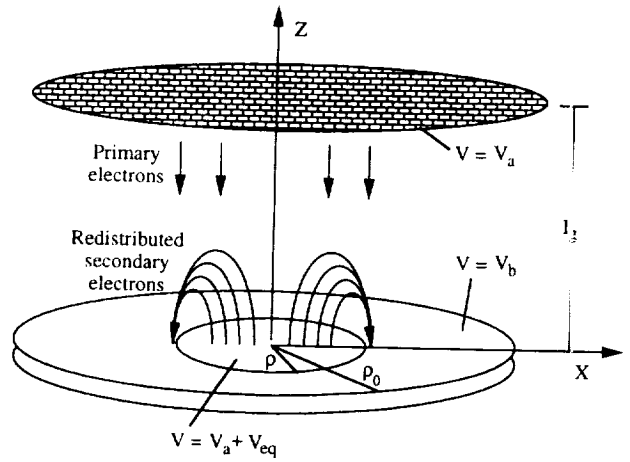
Fig. 6. Redistribution of secondary electrons caused by transverse fields.

shows how electrons emitted with E_s of 2–3 eV are attracted by the relatively high potential of the undeposited region. For typical patterns such as the circle shown with $\rho = 2.5$ mm, deposited in an active area with $\rho_0 = 8$ mm, the energy required for a secondary to reach the grid before it is accelerated back to the undeposited region is in the range $E_{s,\mathrm{m\,n}} \approx$ 10 eV to $E_{s,\mathrm{min}} \approx 100$ eV, with the higher energies required for secondaries emitted near the edge of the pattern. These values are considerably greater than the average secondary-electron energy. This implies that redistribution begins to occur when the gap voltage V_g is reduced by charge accumulation to below ~ 100 V.

The fraction of secondary electrons collected at the grid, implicitly assumed in subsection 2.A to be given by $\delta_c = \delta_e$, is reduced by redistribution to $\delta_c \approx 0$. This conclusion results in the prediction that the total charge accumulated on the surface of the mirror grows approximately linearly with time,

$$Q_{\mathrm{net}} \approx I_p t, \tag{7}$$

directly proportional to the primary current. Further, the deposited area grows linearly with time as

$$A_{\mathrm{depo}} \approx \frac{I_p t}{\sigma_{\pi\ 2,R}}. \tag{8}$$

C. Experimental Behavior of Charge Spread

The conclusion entailed in relation (8) is easily tested by uniform illumination of a test pattern onto the MSLM photocathode and by recording of the size of the output produced as a function of time. Figure 7 shows the results for a test pattern consisting of a 3-mm-diameter circle centered in the 16-mm-diameter active area of the MSLM. In the images shown in the figure the camera's CCD array is inscribed in the circular MSLM active area. The edges of the MSLM crystal are just visible in the corners of the images. Figure 7(a) shows the pattern after the
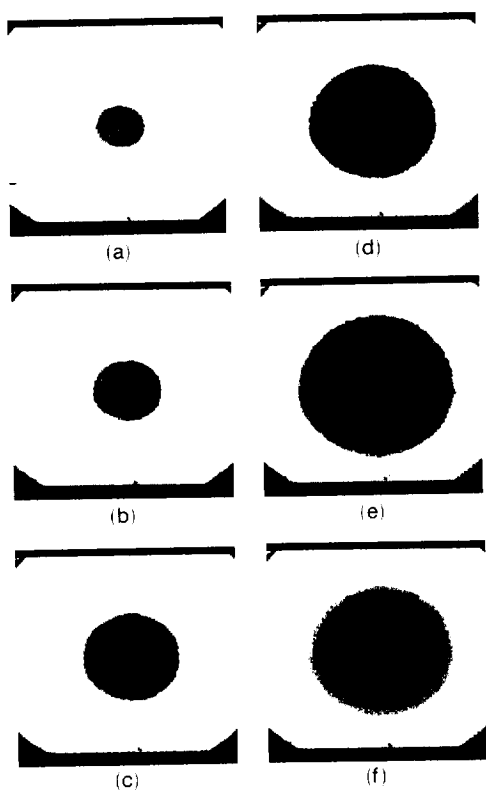
Fig. 7. Spread of a 3-mm-diameter circular test pattern during electron-deposition-mode writing: (a) pattern after writing time t_1 given by Eq. (9); (b) pattern after time $2t_1$, (c) $4t_1$, (d) $8t_1$, (e) $16t_1$; (f) average of 17 images of MSLM output taken from t_1 to $16t_1$ at equal intervals.

writing time

$$t_1 = \frac{\sigma_{\pi/2,R} A_0}{I_p}, \tag{9}$$

where A_0 is the area of the circle. The pattern begins to expand with continued electron deposition, with the results for $t_2 = 2t_1$, $t_3 = 4t_1$, $t_4 = 8t_1$, and $t_5 = 16t_1$ shown in Figs. 7(b)–7(e). The area written by the primary beam is held constant throughout this procedure. The radius of the circle at $t = t_3 = 4t_1$ is almost exactly twice that at t_1. At $t = t_5 = 16t_1$ the radius has grown by a factor of 3.5.

These results imply that δ_c remains nearly zero until charge has accumulated to $\sigma_{\pi/2,R}$ over a large fraction of the MSLM active area. After charge has been deposited over a large fraction of the active area, δ_c becomes appreciable but is still less than unity. The entire active area is eventually written over by charge deposition. As mentioned in the introduction, the spread of a pattern written on an MSLM in electron-deposition mode has been treated in the past as an artifact. In Section 3 we describe an application in which continuous two-dimensional functions are used that are most easily calculated with algorithms involving the spread of information from one location to another.

3. Robot Path Planning Using Potential Fields

Robotic systems include a variety of mechanical devices, such as wheeled vehicles, manipulator arms, multifingered hands, and free-flying platforms. In general, some or all of a robot's motions are controlled automatically by means of computer commands. While many lower level actions, such as the bending of a manipulator arm joint, have long been fully automated, higher level functions have required the participation of a human operator. One such higher level function is the determination of a robot's motion through its environment. The robot's workspace may be partially filled with obstacles, regions that it cannot traverse because of physical or other constraints.

An excellent introduction to the field of autonomous robotic path planning may be found in Ref. 15. Here we consider one class of path-planning problem, that of determining a series of motions for a robot to execute to move from an initial location to a designated goal location in a bounded two-dimensional workspace. Figure 8(a) shows what would be a view from above of such a workspace. In the figure the workspace is bounded to a square region and contains some number of obstacles, represented as filled geometric shapes in the figure. A simple example would be a room bounded by walls and containing furniture of various shapes. Our problem is defined as the
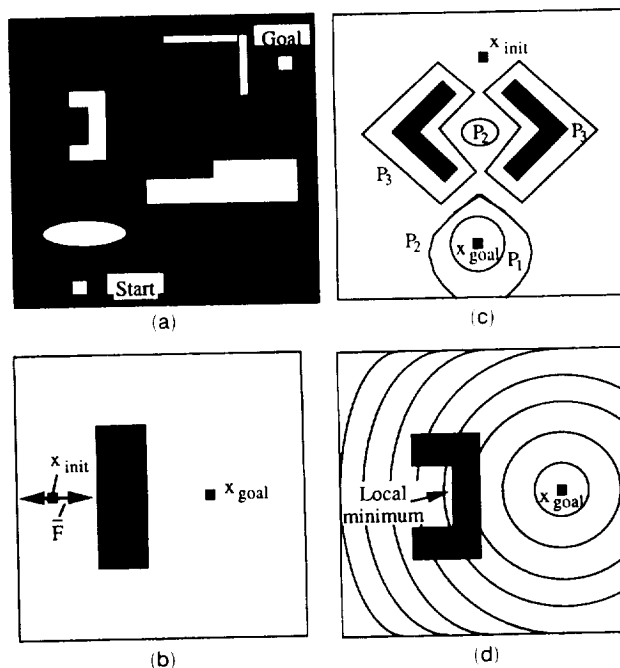

Fig. 8. Bounded two-dimensional workspace containing obstacles: (a) example initial and goal locations for a mobile robot, (b)–(d) local minima in potential-field maps. In (b) the force on the robot directly behind the obstacle is completely perpendicular to the obstacle surface, and the robot cannot move around the obstacle. In (c) the repulsive force from two obstacles forms a local minimum between them at $P_2 < P_3$. In (d) the superposition of potential caused by the goal with a high-potential obstacle results in a local minimum behind the obstacle.

guiding of the robot from its initial position, x_{init}, to a goal, x_{goal}, determined either by its own reasoning system or an outside agent.

Many types of path-planning algorithm have been investigated.[15] A general distinction can be made between those that attempt to find an optimal path, for instance, a minimal-distance path, and those that attempt to find an efficient, if not provably optimal, path. We consider here the method of path planning that uses artificial potential fields, which falls into the second category. In the potential-field method[16–21] each location in the workspace is considered to have an associated potential energy $U(x)$. In practice the workspace is usually divided into some finite number of cells. Each cell has a distinct potential value, and the robot moves in discrete jumps from cell to cell. The robot is assumed to follow the gradient of the potential, responding to the force

$$\overline{F}(x) = -\overline{\nabla}\,\overline{U}(x). \tag{10}$$

Other much more sophisticated algorithms for choosing the path have also been developed,[15–21] but in all cases a method is needed for calculation of a potential value for each cell.

The potential-field technique takes its name from its use of an analogy to electrostatic potentials. The robot is assumed to be a positively charged object, the goal is a negatively charged region that exerts an attractive force, and obstacles are positively charged regions that exert repulsive forces on the robot. Generally the field throughout the workspace caused by each obstacle and the goal are calculated separately and then added to produce a potential-field map for the entire workspace. The actual functional form of U can follow the electrostatic analogy of a field that is inversely proportional to distance, but more usually the form of $U(r)$ is not exactly $1/r$ but is some other monotonically decreasing (in amplitude) function.[15,19–21]

The biggest drawback of the potential-field approach is that it often produces local minima that can trap the robot before it reaches the goal.[15] Figure 8(b) shows this for a workspace containing a single simple obstacle. At a point directly behind the obstacle from the goal the force on the robot is either directly away from or toward the obstacle, or the robot may reach a local minimum in which the forces exactly cancel. A second problem can arise because of the use of positive potential-field contributions from obstacles. Figure 8(c) shows three levels of equipotential lines, with values $P_3 > P_2 > P_1$, for a work space containing two obstacles. The edges of the obstacles that are close together form a high-potential ridge (at potential value P_3 in the figure) that forms a local minimum between them (at potential P_2). The second cause of local minima can be eliminated by use of a spatially extending potential only for the goal. The obstacles are still maximum-potential locations, but they have no field that extends beyond their boundaries. This solution causes its own problems with local minima, however, as shown in Fig. 8(d). As the potential monotonically decreases the closer the robot gets to the goal, the robot will head straight for the goal until it hits an obstacle, and it will then slide along the obstacle until it either slides around the obstacle's edge or is trapped in a local minimum behind it.

A recent technique avoids all three local minima situations in Fig. 8 by calculating potential values for the entire workspace as a system instead of by calculating independent contributions from the goal and obstacles separately and adding them together.[22] As in Fig. 8(d), the obstacles are considered maximum-potential regions that do not exert forces beyond their boundaries. The goal location is the source of an expanding low-potential region that starts in a small area and grows uniformly until it reaches an obstacle. Upon reaching an obstacle the goal's field expands around the obstacle. The field stops expanding when it has filled the entire workspace.

Figure 9 shows the steps in this process, beginning with the original obstacle and the goal location in Fig. 9(a). In Fig. 9(b) the first two equipotential lines surrounding the goal are shown. In this algorithm each equipotential line is separated by an equal distance. After the obstacle is reached, the equipotential lines are no longer radially symmetric but are distorted in going around the object, as shown in Fig. 9(c). The completed pattern in Fig. 9(d) contains no local minima, and a robot located behind the obstacle is guided around it by following a path generated with
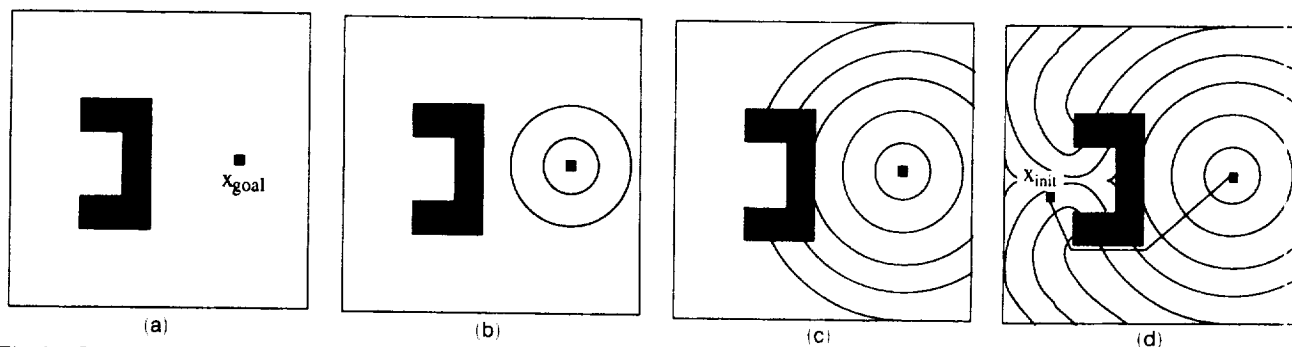

Fig. 9. Potential-field map calculation algorithm employing an expanding goal region: (a) initial goal and obstacle locations, (b) first two equipotential lines showing the expanding goal region, (c) expanding goal region that is forced to proceed around obstacles, (d) final equipotential map. Highest potentials are directly behind the obstacle.

a simple gradient-descent algorithm, such as the path shown in the figure. In a conventional digital electronic implementation, this algorithm runs in $O(N^3 {}^2)$ time, where N is the number of cells.[22] Alternative techniques for overcoming local minima depend on algorithms for avoiding local minima during traversal of the potential-field map. These algorithms are more computationally intensive than simple gradient descent.[15,19,20]

4. Optical Calculation of Potential Fields

A general drawback with robotic path planning by use of potential fields is the large amount of computation necessary to produce paths that are not distorted by local minima. In many cases one desires to calculate paths for a robot operating in a dynamic environment.[15,16] The obstacles in the workspace may be moving, and there may be multiple robots, each of which acts as a potentially moving obstacle to the others. A rapid method of calculating local minima-free potential-field maps could enable dynamic path re-planning, especially for large, high-resolution workspaces.

A. Optical Computation Algorithm

A potentially high-speed analog optical calculation of field maps suitable for robotic path planning can be performed with a microchannel spatial light modulator. In Section 3 an algorithm was given for computing potential-field maps that involved distinct, sharp-edged obstacles and an expanding goal area. The two write modes of the MSLM may be used to implement both types of behavior.

The algorithm is diagrammed in Fig. 10. Let the workspace be represented by the output pattern of the MSLM. The workspace is initially uniformly written in depletion mode, and then the goal is written in deposition mode. At this point an image of the MSLM output shows the goal at a value of zero, while the remaining area of the workspace is at the maximum 8-bit gray-scale value of 255. A series of alternating deposition–depletion writing cycles follows. The goal region is written for a time t_c, during which time the deposited region expands following Eq. (8), by

$$\Delta A \approx \frac{I_p t_e}{\sigma_\pi {}_{2,R}}. \tag{11}$$

When the expanding deposited area reaches the location of an obstacle, some of the area written through Eq. (11) falls within the borders of the obstacle. One removes this charge by writing in depletion mode for a time t_p. All obstacles are written back to full intensity before an image is taken of the output pattern. The procedure terminates after the area written to full modulation by electron deposition spreads to cover the entire active area of the electro-optic crystal, excluding the regions occupied by obstacles. When the workspace is fully written, output images no longer change, and the cycle is stopped.
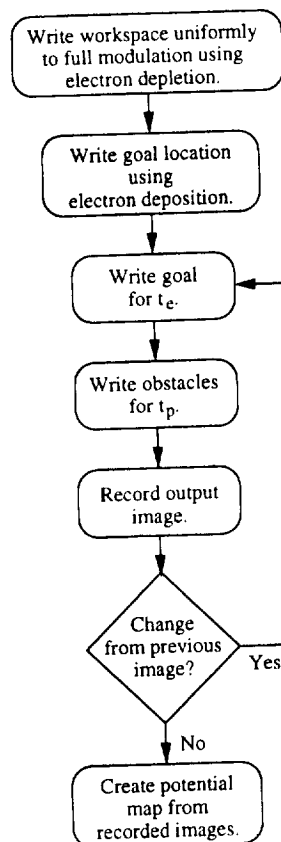

Fig. 10. Algorithm for optical calculation of the potential-field map with both electron deposition and depletion write modes of the MSLM.

The potential-field map is formed by averaging of the images taken at the end of each deposition–depletion write cycle, and it should contain no local minima. Any electrons that spread into the bounds of obstacles are removed, while electrons that spread around the edges of the obstacles are permitted to accumulate. Eventually the deposited area should spread around obstacles, creating a potential map similar to that in Fig. 9.

Experimentally, the algorithm in Fig. 8 does not terminate as desired. The deposited pattern, instead of spreading all the way around the obstacle, spreads only part way and then reaches an equilibrium state such as that shown in Fig. 11. This results from the nonisotropic transverse forces felt by secondary electrons. The primary electrons continue to strike the dielectric mirror in the spatial pattern of the original goal. When expansion begins, secondary electrons are affected by relatively uniform transverse forces, and the goal expands in all directions. After the deposited area reaches the obstacle and begins to expand around it, the electrostatic forces that affect the secondaries impel them preferentially to the region of the obstacle. An equilibrium is reached when all the charge deposited in one deposition period falls within the borders of the obstacle and is removed during the following depletion period. This is shown in Fig. 11(b), in which the deposited
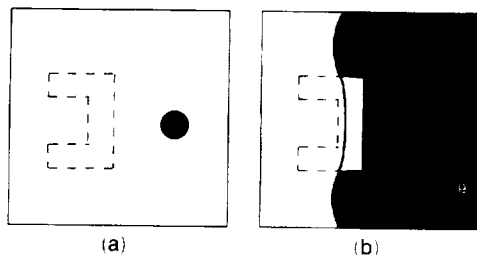
Fig. 11. Premature termination of optical potential-field calculation algorithm: (a) initial locations of the obstacle and the goal, (b) equilibrium state. During the deposition portion of the write cycle, electrons are deposited up to the solid curve. These newly deposited electrons are removed during the immediately following electron-depletion portion of the cycle.

pattern expands up to the solid curve during deposition. When the obstacle is rewritten in depletion mode, all of this charge is removed.

B. Optical Feedback

The unwanted equilibrium in Fig. 11 results from continual deposition of a relatively small amount of charge in a fixed pattern, even after the deposited region has grown dramatically. This procedure is not the best analogy to the potential-field calculation algorithm discussed in Section 3 and shown in Fig. 9. In that algorithm the region of cells for which a potential value is calculated spreads from the edge out. A better optical analogy is to deposit charge over the entire region that is already fully modulated by electron deposition. For instance, for the pattern in Fig. 11(b), during the next electron-deposition step we wish to illuminate the photocathode in all areas that are already dark in the figure. In this way we guarantee that not all secondary electrons emitted

during deposition writing are attracted to the obstacle region. Some are emitted much nearer to other, nonobstacle, depleted areas, and the deposited region continues to grow until the entire workspace is filled.

The procedure for creating a potential-field map with optical feedback is exactly the same as that given in Fig. 8, with the command write goal for t_e replaced with the command write feedback for t_e. The algorithm was tested with the experimental apparatus diagrammed in Fig. 12. The collimated laser beam is split into a readout beam and a write beam. The readout light is polarized at 45° to the $LiNbO_3$-crystal x axis. After passing through the electro-optic (EO) crystal, the readout beam is divided into an output and a feedback beam by the polarizing beam splitting cube, BS3. The polarizing cube passes the output pattern in one direction, and this beam is imaged onto the Cohu Model 6500 CCD camera by lens L1 without the requirement of an additional analyzer, as BS3 itself acts as the analyzer. The second beam from BS3 is the inverse of the output pattern.

Shutters triggered by the Technology Advancement Group (TAG) Model M3 MSLM controller determine whether the write beam or the feedback beam is incident upon the MSLM photocathode. The write beam is modulated by a transparency that represents the obstacle pattern. The feedback and the obstacle patterns are imaged onto the MSLM photocathode by lenses L2 and L3. The TAG controller triggers shutter S2 to open at the same time that it drops the crystal voltage, V_b, to effect electron-deposition writing. During electron deposition, V_b remains high and S1 is open. After each deposition–depletion write cycle, an image is taken by the frame grabber on a MASSCOMP 5600 computer. In a fully developed
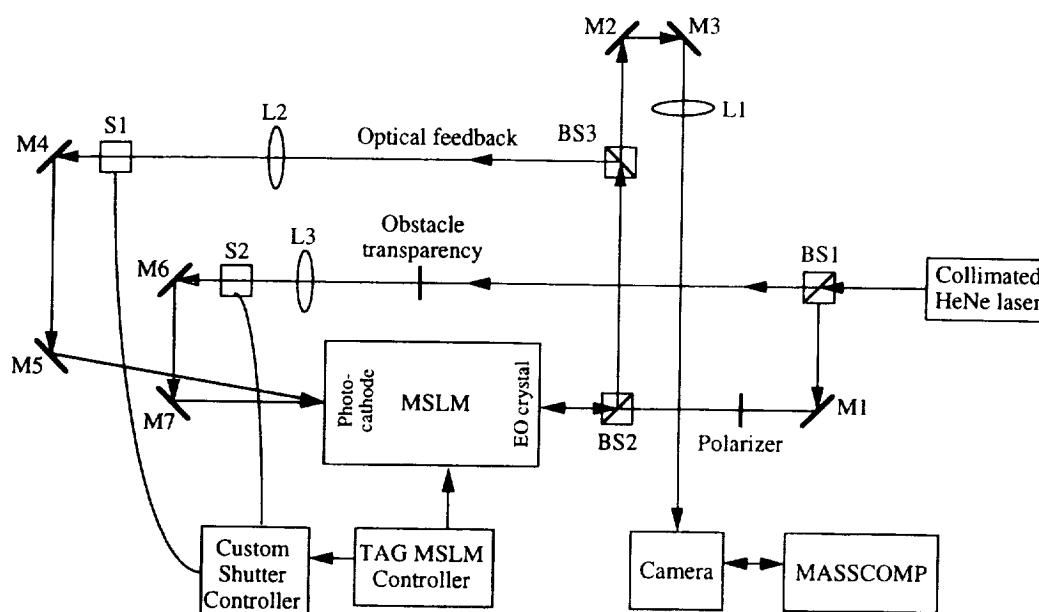

Fig. 12. Experimental apparatus for execution of the optical potential-field calculation and algorithm that uses feedback. The inverse of the current MSLM output is optically fed back and imaged on the photocathode. The polarizing beam splitting cube BS3 separates the output and the feedback patterns. M1–M7, mirrors.

system the MSLM controller would itself be under computer control, and the entire algorithm would be executed automatically. In these experiments the loop was not closed between the computer and the MSLM controller. The MCP was turned off manually by use of the MSLM controller after each write cycle, and a frame grab was manually initiated before the next write cycle.

In practice, direct optical feedback fails to produce useful potential patterns. The problem in this case results from small, dimly illuminated areas in the feedback light distribution that are caused by the finite contrast of the MSLM and the polarizing beam splitting cube. These areas build up rapidly and can overwrite large areas of the workspace before the goal area has a chance to spread significantly.

C. Electronic–Optical Feedback

Direct feedback from the MSLM output to its input fails because of the reinforcement that feedback gives to noise. This problem can be greatly reduced by thresholding of the feedback pattern to remove dimly illuminated areas. Thresholding could be performed optically with either a second MSLM or a Hughes liquid-crystal light valve.[23] Here we take advantage of the fact that we already take images of the MSLM output with a frame grabber and store them digitally on a computer. For little additional digital computation the images can be inverted, thresholded, and displayed on an electronically addressed spatial light modulator (SLM). The revised optical potential-field calculation algorithm is diagrammed in Fig. 13.

The modified experimental apparatus is shown in Fig. 14. The nonpolarizing beam splitting cube, BS3 in Fig. 12, is removed and replaced by a separate write beam illuminating a magneto-optic SLM (MOSLM).[24] The MOSLM implements a 128 × 128 pixel binary amplitude pattern to modulate the feedback light beam and is controlled by the MASSCOMP computer. The 9.1-mm-wide MOSLM aperture is imaged by lens L2 with a magnification of 1.25×. With this magnification the MOSLM aperture is inscribed in the 16-mm-diameter circular active area of the MSLM. In practice we are able to resolve 5–6 line pairs/mm with the MSLM, which is sufficient at this magnification to resolve single MOSLM pixels.

D. Proposed Use of Electron-Beam-Addressed Spatial Light Modulator

The apparatus in Fig. 14 could be greatly simplified by the use of an electron-beam-addressed SLM (EBSLM).[25–26] The EBSLM modulates light in the same manner as the MSLM, through the placement of a charge distribution on the backplane of an electro-optic crystal. Instead of using an optically addressed photocathode, the EBSLM writes with an electron beam; it is essentially a cathode ray tube with the phosphor screen replaced by a $LiNbO_3$ crystal. Figure 15 shows that much of the optics and space necessary in Fig. 14 to implement optical potential-field calculations can be eliminated with an EBSLM. Both the feedback pattern and obstacle pattern can be
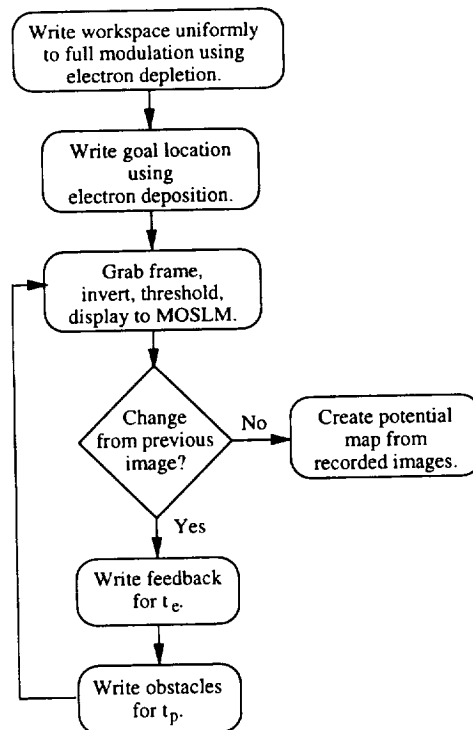

Fig. 13. Algorithm for optical calculation of a potential-field map that uses optical feedback of an inverted, thresholded MSLM output image. The feedback pattern is written during the deposition-mode portion of each write cycle. A fixed-obstacle pattern is written during the depletion-mode portion.

written directly from the controlling personal computer (PC). Only the readout optics are still required.

5. Calculation Time

In this section we first derive the total optical writing time necessary to complete a potential-field calculation. The total duration of MSLM writing, t_{calc}, depends on the number, size, and relative positions of the obstacles present in the workspace. However, we can derive a scaling law independent of obstacle pattern. This permits us to determine the parameters of MSLM design that most strongly affect calculation speed and to estimate the highest speed achievable with current technology.

The potential-field calculation algorithm in Fig. 13 also includes operations that are implemented electronically. The exact values for the time necessary to perform these operations depends on the particular implementation hardware. However, we can compare the scaling of computation time with the size of the robot's workspace for both the electronic and the optical operations in order to determine the ultimate limiting factor for system speed. The scaling factor for the speed of the hybrid optical–electronic system can then be compared with the scaling factor for conventional digital electronic systems.

A. Derivation of Optical Writing Time

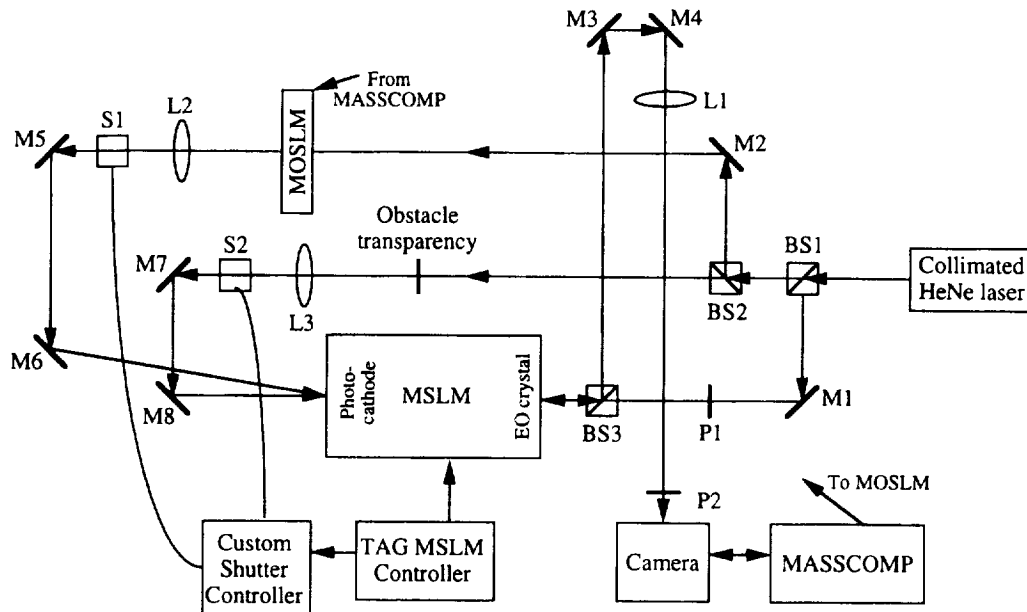First we consider the time necessary to fully modulate the entire active area of the crystal in the case in

Fig. 14. Experimental apparatus for the execution of the optical potential-field calculation algorithm of Fig. 13 with electronic–optical feedback. The current MSLM output is electronically inverted, thresholded, and displayed on the MOSLM. The MOSLM pattern is imaged on the MSLM photocathode and written during the deposition-mode portion of the write cycle.

which no obstacles are present. Full modulation of a readout light beam passing twice through the crystal requires a charge density[4]

$$\sigma_{\pi\ 2,R} = \frac{\epsilon_0\epsilon_{\parallel}\lambda}{4n_0{}^3 r_{13}l_x}, \qquad (12)$$

where $\epsilon_{\parallel}\epsilon_0$ is the permittivity of the crystal along the field direction, λ is the wavelength of the readout light, n_0 is the ordinary refractive index of the crystal, r_{13} is the crystal's electro-optic coefficient, and l_x is the crystal thickness. For LiNbO$_3$ this charge density is minimized for a 55°-cut crystal with $\epsilon_{\parallel} = 36$. With $\lambda = 633$ nm, $n_0 = 2.28$, $r_{13} = 8.6 \times 10^{-12}$ m/V, and $l_x = 50$ μm, $\sigma_{\pi\ 2,R} = 4.2 \times 10^{-3}$ C/m^2, as used in Section 2.
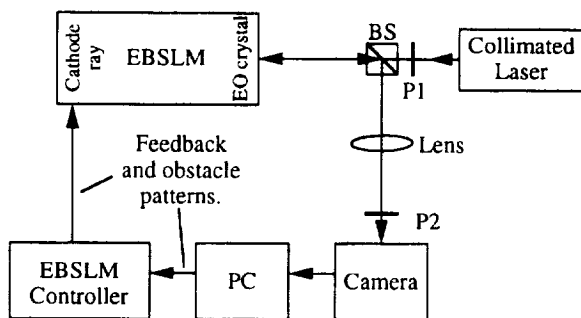

Fig. 15. Proposed apparatus for the execution of the optical potential-field calculation algorithm of Fig. 13 with electronic feedback. Most of the optics required in Fig. 14 is made redundant through the use of an electron-beam addressed SLM (EBSLM). A personal computer (PC) controls the writing of both the obstacle and the feedback patterns. Only readout optics are required.

Assuming a uniform-intensity write beam limited by an aperture of area A, the total charge deposited on the dielectric mirror in a time Δt is given by

$$\Delta Q = J_p A \Delta t, \qquad (13)$$

where J_p is the current density of the primary beam incident upon the mirror and where we assume that almost no secondary electrons are collected at the mesh electrode, i.e., $\delta_c \approx 0$. The deposited charge fully modulates an area given by

$$\Delta A = \frac{\Delta Q}{\sigma_{\pi/2,R}} = \frac{J_p A \Delta t}{\sigma_{\pi\ 2,R}}, \qquad (14)$$

For short writing-time intervals, $\Delta A \ll A$, and Eq. (14) may be rewritten as

$$\frac{dA}{dt} = \frac{J_p A}{\sigma_{\pi/2,R}}. \qquad (15)$$

Equation (15) has the solution

$$A = A_0 \exp\left(\frac{J_p t}{\sigma_{\pi/2,R}}\right), \qquad (16)$$

where A_0 is the area that is originally written by the primary beam before secondary redistribution occurs; i.e., A_0 is the area of the original goal location. Equation (16) can be rewritten in terms of the time necessary to modulate the entire active area, A_m:

$$t_m = \frac{\sigma_{\pi/2,R}}{J_p} \ln\left(\frac{A_m}{A_0}\right). \qquad (17)$$

The parameter t_m gives only the electron-deposition

write time. The potential-field calculation algorithm requires a period of electron-depletion mode writing, t_p, for each period of deposition, t_c. The write time for electron depletion, or secondary-emission mode, is related to deposition writing time by

$$t_p = t_c \frac{1}{(\delta_s - 1)}, \qquad (18)$$

where δ_s is the secondary-emission coefficient. The modulation time in Eq. (17) must be increased by the factor

$$\eta \equiv 1 + \frac{1}{(\delta_s - 1)} = \frac{\delta_s}{(\delta_s - 1)}. \qquad (19)$$

Following Ref. 5, we use $\delta_s = 1.7$ for SiO_2, giving $\eta = 2.4$. The calculation time in the absence of obstacles is then given by

$$t_{calc,0} = \frac{\eta \sigma_{\pi\ 2,R}}{J_p} \ln\left(\frac{A_m}{A_0}\right). \qquad (20)$$

When obstacles are present, some of the charge accumulated during deposition-mode writing is deposited in obstacle regions. This charge is removed during subsequent depletion-mode rewriting of obstacles, and it does not contribute to modulating all of the obstacle-free regions of the active area. More time is therefore necessary to complete modulation. This is reflected in our final equation for optical writing time:

$$t_{calc} = \frac{\xi \eta \sigma_{\pi\ 2,R}}{J_p} \ln\left(\frac{A_m}{A_0}\right), \qquad (21)$$

where ξ is a factor greater than one that is dependent on the specific number, size, and placement of obstacles in the workspace and also on the position of the goal. An analytical expression for ξ cannot be derived, but it is related to the complexity of the obstacle arrangement. In the experimental results presented in Section 6, ξ is found to vary from less than 2 for a workspace containing a single obstacle to a value of ~3 for a four-obstacle situation.

B. Optical Writing Time Using Current Microchannel Spatial Light Modulators

In spite of the obstacle-dependent parameter, ξ, Eq. (21) tells us much about the attainable optical writing speed of an optical–electronic processing system designed to calculate potential fields for robotic path planning. Let us first consider the shortest time achievable with current devices. We have given values for the parameters $\sigma_{\pi\ 2,R}$ and η from Eqs. (12) and (19). A_m is the area of a 16-mm-diameter circle. The primary-current density is found by multiplication of the MCP output current, i_0, measured when the photocathode is uniformly illuminated, by the electron transmittance of the mesh electrode, α, and

by division by A_m:

$$J_p = i_0 \alpha / A_m. \qquad (22)$$

Current MSLM's are limited to maximum output currents of ~10 μA,[4,5] giving $J_p = 3 \times 10^{-2}$ A/m^2 for $\alpha = 0.6$.[5] The final parameter to be determined is A_0, the original goal area.

It is desirable to specify the area of the goal as the area of a single resolution cell. The modulation transfer function roll-over frequency for an MSLM is approximated by[4,27]

$$\omega_1 \approx \frac{(\epsilon_\parallel/\epsilon_\perp)^{1/2}}{l_x}, \qquad (23)$$

where the crystal resolution parameter $(\epsilon_\parallel/\epsilon_\perp)^{1/2}$ is equal to 0.9 for 55°-cut $LiNbO_3$. Given $l_x = 50$ μm, $\omega_1 = 5.7$ line pairs/mm. Given this resolution, the minimum cell size is

$$A_0 = \left(\frac{1}{2\omega_1}\right)^2 = 7.7 \times 10^{-9} \text{ m}^2. \qquad (24)$$

The result from Eq. (21) for the optical writing time required for the calculation of a full potential-field map with current commercial MSLM's is $t_{calc} = 3\xi$ s, of the order of 10 s for the patterns demonstrated in Section 6. Experimental versions of MSLM's have been demonstrated with MCP output currents as high as 300 μA. Use of such MCP's would decrease t_{calc} to a few tenths of a second, permitting potential-field map updates at a few hertz.

C. Write-Cycle Frequency

The derivation of optical writing time includes both periods of deposition-mode writing lasting t_c and depletion-mode writing for periods of t_p. The ratio of these writing periods is given by Eq. (18), but their specific durations are not used in deriving t_{calc}, although they were assumed to be much shorter than t_{calc} in writing the differential equation of Eq. (15).

The limit on write-cycle duration is determined in practice by the phenomenon referred to as breaching. If the area written in deposition mode is permitted to expand too much before the obstacles are rewritten, deposited electrons can spread completely across an obstacle. The charge that is deposited behind the obstacle remains after the obstacle is rewritten and leads to creation of a local minimum in the final potential field. Figure 16 displays the effect of breaching for a one-obstacle workspace. In Fig. 16(a) the goal region has just expanded to the obstacle, delineated by the dashed lines. If the deposition writing duration t_e is too long, electrons are deposited behind the obstacle, as in Fig. 16(b). After the obstacle is rewritten by use of electron depletion, the pattern in Fig. 16(c) results. As electrons are deposited at point B before they reach point A, point B will have a lower potential than point A, and a robot placed behind the obstacle will become trapped in a local minimum.
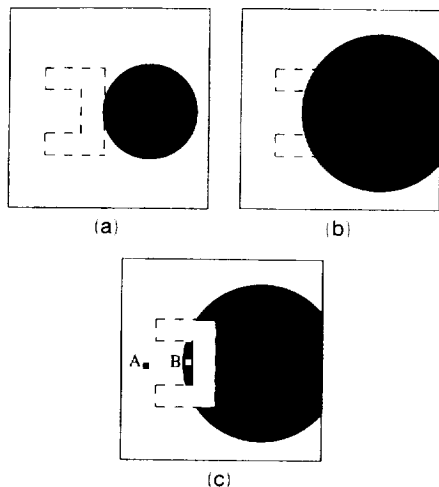
Fig. 16. Obstacle breaching: (a) deposited region has expanded to the edge of an obstacle; (b) if deposition writing duration t_e is too long, the deposited region expands across the obstacle; (c) after the obstacle is rewritten by use of electron depletion, the deposited charge remains behind the obstacle. The final potential at point B will be lower than at point A, resulting in a local minimum.

Breaching does not occur if the total amount of charge deposited during t_e is sufficiently small. The total number of deposition–depletion write cycles performed in one potential-field map calculation is given by

$$M = \frac{t_{calc}}{\eta t_e},$$ (25)

where t_{calc} is given by Eq. (21). For typical obstacles with minimum thicknesses of ~ 0.5 mm we find empirically that M must be of the order of 100 to avoid breaching.

D. Scaling of System Calculation Time and Microchannel Spatial Light Modulator Optimization

In addition to calculation speed we are interested in total computational throughput. The value for t_{calc} computed in Subsection 5.B is for a potential field with 128×128 pixel resolution (more if the full circular aperture of the MSLM were actually used). The number of resolution cells, N, is given by

$$N = A_m/A_0.$$ (26)

Therefore we see from Eq. (21) that the optical writing time scales as

$$t_{calc} \propto \ln(N).$$ (27)

The full potential-field calculation algorithm of Fig. 13 includes the electronically implemented functions of frame grabbing, image thresholding and inversion, and display of a feedback pattern on an electronically addressed SLM. Each of these operations scales linearly with the size of images, i.e., as $O(N)$. In addition, each of these operations is repeated M times during the calculation of a potential-field map.

From Eqs. (21) and (25), M is seen to scale as $O(\ln(N))$. The electronic operations therefore determine the ultimate limit on system computation speed. In the limit of large N, the order of the computation time for the overall optical–electronic system is $O(N \ln(N))$.

We discussed in Section 3 that the calculation of local minima-free potential-field maps with conventional digital electronics scales as $O(N^{3\,2})$. The advantage of optical calculations therefore lies in the domain of large, high-resolution potential-field maps. N may be increased either by an increase in the active area of the crystal or by an increase in the crystal resolution. Equations (23) and (24) show that, aside from the use of alternative crystals, resolution can be increased only by a decrease in the crystal thickness, l_x. A decrease in l_x also increases the optical writing time, as t_{calc} in Eq. (21) is directly related to $\sigma_{\pi\,2,R}$, which is in turn inversely related to l_x from Eq. (12). However, as the minimum resolution cell area A_0 is proportional to $(1/l_x)^2$, a thinner crystal is preferable in terms of total system performance.

6. Experimentally Calculated Fields and Paths

The optical potential-field computation algorithm of Fig. 13 utilizing electronic–optical feedback was tested on three different types of workspace. A workspace with no obstacles was tested first in order to confirm the theoretical derivation of t_{calc} presented in Section 5, and then experiments were performed for both single- and multiple-obstacle workspaces. A low MCP output current of $i_0 = 0.07$ μA, giving $J_p = 2.1 \times 10^{-4}$ A/m² from Eq. (22), and long writing times of $t_e = 2$ s and $t_p = 2.8$ s were used in order to easily control execution of the experiment. This output current is only 0.7% of the current obtainable with this MCP. The apparatus used was that diagrammed in Fig. 14.

A. Confirmation of Theoretical Optical Writing Time

With no obstacles present the rate of growth of the area written in electron-deposition mode was tested by use of feedback, predicted to follow Eq. (16). The derivation of this equation assumed that essentially all secondary electrons emitted are redistributed on the MSLM's dielectric mirror and that very few are collected on the mesh electrode ($\delta_c \approx 0$). The goal area was initially written as a 1.25-mm-diameter circle, $A_0 = 1.2 \times 10^{-6}$ m², centered in the active area of the electro-optic crystal. The result for the area of the crystal written by electron deposition versus time is shown in Fig. 17, normalized to the initial area A_0. Data were taken, and the feedback pattern was updated every 2 s.

A total of $M = 52$ iterations were necessary to complete deposition of the entire active area. The experimental data points are very well with Eq. (16) until almost the entire active area is written. The experimental curve falls below the theoretical curve near the end of the writing process, implying that some secondary electrons are collected on the mesh electrode. This deviation from theory has a negligible effect on the total time necessary to modulate
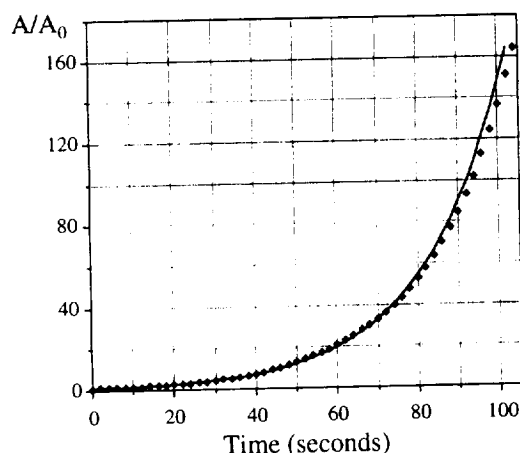
Fig. 17. Exponential growth of the region written with electron deposition by use of electronic–optical feedback. A slight discrepancy between experimental points and theory [the solid curve is from Eq. (16)] is attributable to some secondary electrons' being collected at the mesh electrode.

the active area, increasing t_m by only 2% from the value predicted from Eq. (17).

B. Single-Obstacle Workspace

A common obstacle used in robotics research[15] was used to demonstrate the procedure in the single-
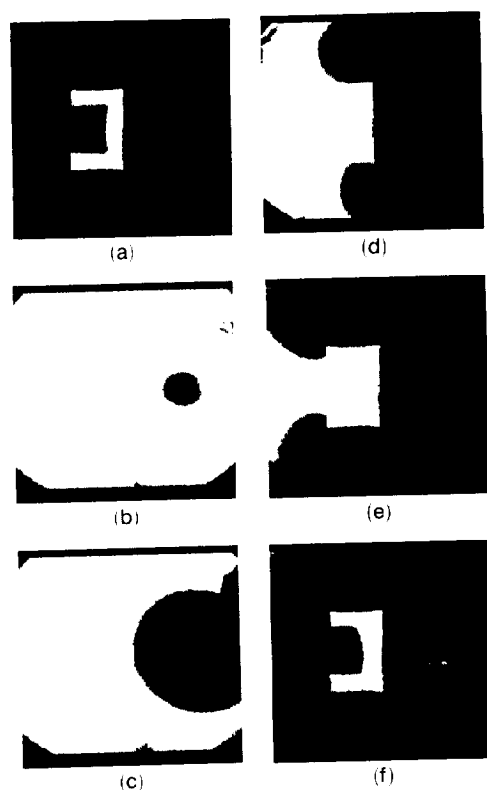

Fig. 18. Intermediate MSLM output images taken during optical potential-field calculation process: (a) C-shaped obstacle, (b) initial goal pattern; (c) output after 20 iterations of deposition-depletion write cycle, (d) 40 iterations, (e) 60 iterations, (f) 80 iterations.
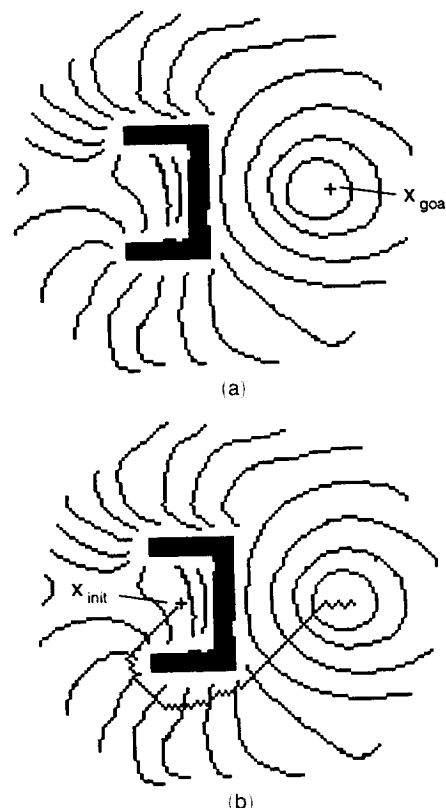

Fig. 19. Optically calculated potential field for the C-shaped obstacle: (a) equipotential contour plot of a gray-scale field map showing goal location, x_{goal}; (b) path followed by a simulated point robot that uses simple gradient descent through the optically calculated potential-field map for the C-shaped obstacle. The path from x_{init} to x_{goal} is roughly perpendicular to equipotential lines.

obstacle case. This is a C- or a U-shaped object, as shown in Fig. 18(a). As noted in Section 3, this type of object is difficult for many path-planning algorithms to handle because of the creation of local minima behind or in the inner space of the obstacle. The obstacle is 1 mm thick, and the goal was initially written as a 1.25-mm circle.

The algorithm required a total of $M = 88$ iterations to complete writing of the entire field. Five intermediate output images are shown in Fig. 18, starting just after the goal was written in Fig. 18(b). Output images after 20, 40, 60, and 80 iterations are shown in Figs. 18(c)–18(f). In Fig. 18(c) the goal region has just expanded to the edge of the obstacle. The deposited area spreads around the obstacle in Figs. 18(d) and 18(e) and almost fills the entire workspace in Fig. 18(f).

The total optical writing time was $M(t_e + t_p) = 420$ s. This compares with the expected value from Eq. (21) of $t_{calc} = 240\xi$ s, giving a value of $\xi = 1.7$. This writing time is much longer than theoretically possible with this MSLM. This experiment was intentionally performed at a low speed because not all steps in the calculation algorithm of Fig. 13 were automated.
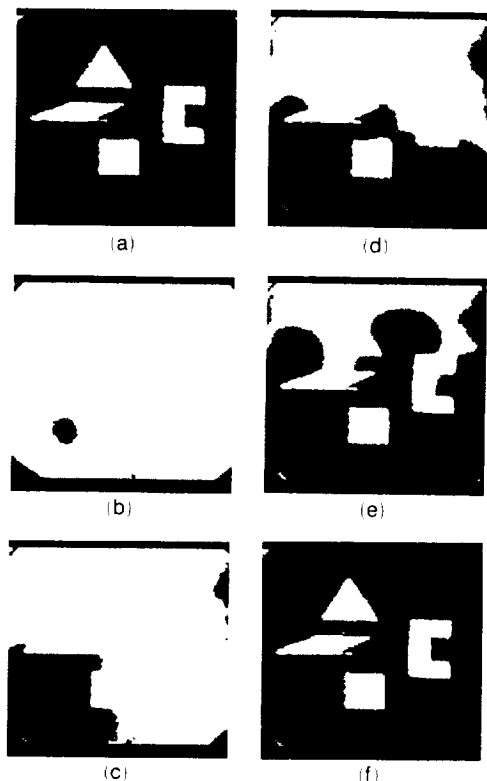
Fig. 20. Intermediate MSLM output images taken during optical potential-field calculation process for a four-obstacle workspace: (a) work space containing triangle, C-shape, square, and parallelogram obstacles; (b) initial goal pattern; (c) output after 40 iterations of the deposition–depletion write cycle, (d) 80 iterations, (e) 120 iterations, (f) 156 iterations.

After the output image stopped changing, the sequence of images stored during the writing process was averaged to produce the potential-field map. The potential-field map is a gray-scale image with values ranging from 0 at the goal to 255 within the bounds of the obstacle. Figure 19(a) shows a contour plot in which the first equipotential line surrounding the goal represents a gray-scale value of 15, and each successive line is separated by a gray-scale value of 16. The highest potential values in the field are those directly behind the obstacle from the goal.

The path that a simple point robot would follow when started at any initial position in the workspace was simulated. A point robot is assumed to occupy only one resolution cell of the workspace at a time. The robot follows the potential map using a simple gradient descent without momentum. It moves from its current location to the adjoining cell with the lowest potential, continuing until it reaches either a local or global minimum.

An example of a path generated for the C-shaped obstacle is shown in Fig. 19(b). The robot is assumed to begin at a location x_{init}, which is behind the obstacle in this case. It then follows a path roughly perpendicular to the equipotential lines. The robot successfully proceeds around the obstacle and reaches the goal without being trapped by any local minima.

In addition, the optically calculated potential field does not result in a path that follows the exact edge of the obstacle. Some potential-field calculation algorithms generate paths that follow obstacle boundaries so closely that a robot with spatial extent beyond one resolution cell would collide with the obstacles.[15]

C. Multiple-Obstacle Workspace

An optical potential-field calculation was also performed for the workspace shown in Fig. 20(a), which contains four obstacles. The calculation process in this case required $M = 156$ write cycles, giving $t_{\text{calc}} = 750$ s and $\xi = 3.1$. Five output images taken during the writing process are shown in Fig. 20, beginning with the initial goal in Fig. 20(b). In Fig. 20(c) the goal region is expanding by three different routes around and between the square and the parallelogram obstacles. The dark area in the upper right-hand corner is caused by MOSLM defects.

The composite potential-field map made from images taken during the writing process is seen in Fig. 21(a), again as a two-dimensional equipotential contour plot. The map shows that the goal region expands most quickly in areas in which there are large gaps between obstacles. The spacing between equipotential lines below the square obstacle is larger than that between lines in the gap between the square and the parallelogram and that between the parallelo-
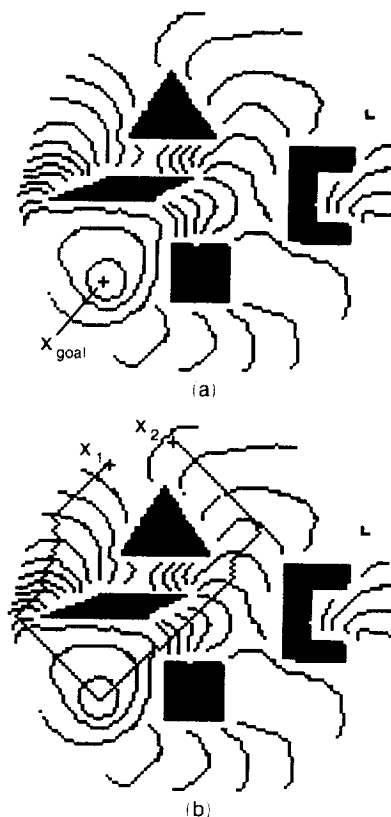

Fig. 21. Optically calculated potential-field for a four-obstacle workspace: (a) equipotential contour plot of gray-scale potential-field map, (b) two paths with different starting positions followed by a simulated point robot that uses simple gradient descent.

gram and the workspace boundary. Near small gaps, a larger percentage of secondary electrons are deposited in obstacle regions and are subsequently removed, resulting in slower spread of the deposited area. Faster spread through large gaps yields potential-field maps that favor robot paths between widely separated obstacles over path of equal length between closely spaced obstacles. In many cases, especially for nonpoint, extended robots, this may be a desirable behavior.[15,22]

An example is shown in Fig. 21(b) that plots two paths generated by use of the potential-field map, again with a simple gradient-descent planning algorithm. The charge-deposited region spreads around the triangular obstacle from two different directions, forming a relatively high potential ridge above and to the left of the triangle. A robot placed on one side of the ridge, such as point x_1 in Fig. 21(b), follows a path in one direction around the triangle and parallelogram, while a robot placed at x_2 on the other side of the potential ridge follows a path in a different direction. The optically generated field map does not guarantee an optimally short path, but it does implicitly weigh the benefits of path length and width and produces a path that represents a compromise between these benefits.

7. Conclusions

The microchannel spatial light modulator has two principle writing modes, which employ either the deposition or the depletion of spatial charge distributions on the surface of an electro-optic crystal. The two modes behave differently when patterns are written past the point of full modulation, with deposited patterns spreading well beyond the area in which the MCP current is incident upon the crystal, while depleted patterns remain relatively confined. This difference is primarily caused by redistribution of electrons produced through secondary emission. These low-energy electrons are attracted by transverse fields to the edge of regions on the crystal surface on which charge has not been deposited.

It has experimentally been shown that the writing-mode characteristics of the MSLM can be used to calculate local minima-free potential-field maps suitable for robotic path planning. Optics is well suited for this application because the hybrid optical-electronic calculation scales as $O(N \ln(N))$, where N is the number of the resolution cells in the robot's workspace, whereas conventional digital electronic calculation of local minima-free maps scales as $O(N^{3/2})$. In addition, optically calculated potential fields have the often desirable characteristics of producing paths through the middle of gaps between obstacles and paths that give preference to wide gaps.

The bandwidth of optical potential-field calculations may be increased most easily by an increase in the area of the electro-optic crystal. Decreasing the crystal thickness also increases the bandwidth, as the increase in resolution more than compensates for increased writing time when one considers a two-dimensional calculation. Further research aimed at optimizing MSLM technology for this application is warranted, as is research into the possibility of performing similar calculations with alternative SLM technologies.

References

1. C. Warde, A. D. Fisher, D. M. Cocco, and M. Y. Burmawi, "Microchannel spatial light modulator," Opt. Lett. 3, 196–198 (1978).
2. A. D. Fisher, "Techniques and devices for high-resolution adaptive optics," Ph.D. dissertation (Massachusetts Institute of Technology, Cambridge, Mass., 1981).
3. C. Warde, A. M. Weiss, A. D. Fisher, and J. I. Thackara, "Optical information processing characteristics of the microchannel spatial light modulator," Appl. Opt. 20, 2066–2074 (1981).
4. C. Warde and J. Thackara, "Operating modes of the microchannel spatial light modulator," Opt. Eng. 22, 695–703 (1983).
5. T. Hara, M. Sugiyama, and Y. Suzuki, "A spatial light modulator," Adv. Electron. Electron. Phys. 64B, 637–647 (1985).
6. T. Hara, Y. Ooi, T. Kato, and Y. Suzuki, "Microchannel spatial light modulator with improved resolution and contrast ratio," in Nonlinear Optics and Applications, P. A. Yeh, ed., Proc. Soc. Photo-Opt. Instrum. Eng. 613, 153–157 (1986).
7. T. Hara, Y. Ooi, Y. Suzuki, and M. H. Wu, "Transfer characteristics of the microchannel spatial light modulator," Appl. Opt. 28, 4781–4786 (1989).
8. A. D. Fisher, W. L. Lippincott, and J. N. Lee, "Optical implementations of associative networks with versatible adaptive learning capabilities," Appl. Opt. 26, 5039–5054 (1987).
9. M. Ishikawa, N. Mukohzaka, H. Toyoda, and Y. Suzuki, "Optical associatron: a simple model for optical associative memory," Appl. Opt. 28, 291–301 (1989).
10. F. T. S. Yu, X. J. Lu, Y. Suzuki, and M. Wu, "Microchannel spatial light modulator with white light processing," Opt. Commun. 63, 371–374 (1987).
11. S. Lau and C. Warde, "Bistable configurations of the microchannel spatial light modulator," Appl. Opt. 27, 2954–2959 (1988).
12. A. Yariv, Introduction to Optical Electronics, 2nd ed. (Holt, Rinehart & Winston, New York, 1976), pp. 246–253.
13. A. M. Tyutikov and L. B. Tsoi, "The distribution, in energy and direction, of the electrons leaving microchannel plates," Sov. J. Opt. Technol. 43, 86–88 (1976).
14. B. Kazan and M. Knoll, Electronic Image Storage (Academic, New York, 1968).
15. J. C. Latombe, Robot Motion Planning (Kluwer, Norwell, Mass., 1991).
16. O. Khatib, "Real-time obstacle avoidance for manipulators and mobile robots," Int. J. Robotics Res. 5, 90–98 (1986).
17. F. Miyazaki and S. Arimoto, "Sensory feedback based on the artificial potential for robots," presented at the Ninth Meeting of the International Federation for Automatic Control, Budapest, 1984.
18. V. V. Pavlov and A. N. Voronin, "The method of potential functions for coding constraints of the external space in an intelligent mobile robot," Soviet Autom. Control 6 (1984).
19. D. E. Koditschek, "Exact robot navigation by means of potential functions: some topological considerations," presented

at Institute of Electrical and Electronic Engineers the International Conference on Robotics and Automation, Raleigh, N.C., 1987.

20. J. Barraquand and J. C. Latombe, "Robot motion planning: a distributed representation approach," Int. J. Robotics Res. **10**, 628–649 (1991).

21. Y. K. Hwang and N. Ahuja, "A potential field approach to path planning," IEEE Trans. Robotics Autom. **8**, 23–32 (1992).

22. E. S. Plumer, "Neural network structure for navigation using potential fields," presented at the International Institute of Electrical and Electronics Engineers–International Neural Network Society Joint Conference on Neural Networks, Baltimore, Md., 7–11 June 1992.

23. W. P. Bleha, L. T. Lipton, E. Wiener-Avnear, J. Grinberg, P. G. Reif, D. P. Casasent, H. B. Brown, and B. V. Markevitch, "Application of liquid crystal light valve to real time optical data processing," Opt. Eng. **17**, 371–384 (1978).

24. J. A. Davis and J. M. Waas, "Current status of the magneto-optic spatial light modulator," in *Spatial Light Modulators and Applications III*, U. Efron, ed., Proc. Soc. Photo-Opt. Instrum. Eng. **1150**, 27–43 (1990).

25. A. Schwartz, X-Y. Wang, and C. Warde, "Electron-beam-addressed microchannel spatial light modulator," Opt. Eng. **24**, 119–123 (1985).

26. K. Shinoda and Y. Suzuki, "Electron beam addressed spatial light modulator," in *Nonlinear Optics and Applications*, P. A. Yeh, ed., Proc. Soc. Photo-Opt. Instrum. Eng. **613**, 158–164 (1986).

27. W. R. Roach, "Resolution of electro-optic light valves," IEEE Trans. Electron. Devices **ED-21**, 453–459 (1974).